

University of Groningen

Substructures, resonances, and debris streams

Dodd, Emma; Helmi, Amina; Koppelman, Helmer H.

Published in:
Astronomy and astrophysics

DOI:
[10.1051/0004-6361/202141354](https://doi.org/10.1051/0004-6361/202141354)

IMPORTANT NOTE: You are advised to consult the publisher's version (publisher's PDF) if you wish to cite from it. Please check the document version below.

Document Version
Publisher's PDF, also known as Version of record

Publication date:
2022

[Link to publication in University of Groningen/UMCG research database](#)

Citation for published version (APA):

Dodd, E., Helmi, A., & Koppelman, H. H. (2022). Substructures, resonances, and debris streams: A new constraint on the inner shape of the Galactic dark halo. *Astronomy and astrophysics*, 659, [A61]. <https://doi.org/10.1051/0004-6361/202141354>

Copyright

Other than for strictly personal use, it is not permitted to download or to forward/distribute the text or part of it without the consent of the author(s) and/or copyright holder(s), unless the work is under an open content license (like Creative Commons).

The publication may also be distributed here under the terms of Article 25fa of the Dutch Copyright Act, indicated by the "Taverne" license. More information can be found on the University of Groningen website: <https://www.rug.nl/library/open-access/self-archiving-pure/taverne-amendment>.


Take-down policy

If you believe that this document breaches copyright please contact us providing details, and we will remove access to the work immediately and investigate your claim.

Downloaded from the University of Groningen/UMCG research database (Pure): <http://www.rug.nl/research/portal>. For technical reasons the number of authors shown on this cover page is limited to 10 maximum.

Substructures, resonances, and debris streams

A new constraint on the inner shape of the Galactic dark halo

Emma Dodd¹ , Amina Helmi¹, and Helmer H. Koppelman²

¹ Kapteyn Astronomical Institute, University of Groningen, Landleven 12, 9747 AD Groningen, The Netherlands
e-mail: dodd@astro.rug.nl

² School of Natural Sciences, Institute for Advanced Study, Princeton, NJ 08540, USA

Received 20 May 2021 / Accepted 9 December 2021

ABSTRACT

Context. The local stellar halo of the Milky Way contains the debris from several past accretion events.

Aims. Here we study in detail the structure and properties of nearby debris associated with the Helmi streams, which was originally identified as an overdensity in integrals of motion space.

Methods. We use 6D phase-space information from *Gaia* EDR3 combined with spectroscopic surveys, and we analyse the orbits and frequencies of the stars in the streams using various Galactic potentials. We also explore how the Helmi streams constrain the flattening, q , of the Galactic dark matter halo.

Results. We find that the streams are split into substructures in integrals of motion space, most notably into two clumps in angular momentum space. The clumps have consistent metallicity distributions and stellar populations, supporting a common progeny. In all the realistic Galactic potentials explored, the Helmi streams' stars depict a diffuse distribution close to $\Omega_z/\Omega_R \sim 0.7$. At the same time, the reason for the substructure in angular momentum space appears to be a $\Omega_z:\Omega_\phi$ resonance close to 1:1. This resonance is exactly 1:1 in the case where the (density) flattening of the dark halo is $q = 1.2$. For this halo shape, the substructure in angular momenta is also long-lasting.

Conclusions. Our findings suggest that the structure of the Galactic potential leaves a clear imprint on the properties of phase-mixed debris streams.

Key words. Galaxy: kinematics and dynamics – Galaxy: halo – Galaxy: structure

1. Introduction

Thanks to *Gaia* data (Gaia Collaboration 2018), the debris of several mergers has recently been unequivocally identified in the halo near the Sun, such as the dominant *Gaia*-Enceladus (Belokurov et al. 2018; Koppelman et al. 2018; Helmi et al. 2018, with possible earlier hints in Chiba & Beers 2000; Brook et al. 2002; Meza et al. 2005; Nissen & Schuster 2010; Hayes et al. 2018). We refer the reader to Sect. 4.2.1 of Helmi (2020) for historical context regarding the discovery of *Gaia*-Enceladus. Other confirmed or newly discovered substructures include the Helmi streams (Helmi et al. 1999; Koppelman et al. 2019a), Sequoia (Myeong et al. 2019), and Thamnos (Koppelman et al. 2019b). Farther out in the halo, the proposed debris of several smaller mergers has also been identified: Wukong, Aleph, I'toi and Arjuna (see Naidu et al. 2020, although Arjuna is plausibly related to *Gaia*-Enceladus, see Naidu et al. 2021). The basic concept behind the identification of phase-mixed debris from accreted galaxies is that they are apparent as clumps in the integrals of motion space, such as energy and angular momenta, even long after the merger is completed (Helmi & de Zeeuw 2000).

Not all substructure, however, has an accreted origin. The Sagittarius dwarf galaxy seems to be the cause of a large amount of substructure, such as the phase spiral (Antoja et al. 2018), ridges in V_ϕ - R space (Ramos et al. 2018; Laporte et al. 2019), and several low-latitude overdensities (e.g. the Monoceros Ring;

Laporte et al. 2018). Meanwhile, the rotating bar at the centre of our galaxy is, for example, the cause of the Hercules stream in the nearby disc (Dehnen 2000), and it also has an impact on the morphology of the stream originating in the halo globular cluster Pal 5 (Pearson et al. 2017).

These last substructures are induced by time-dependent effects that cause changes in a star's orbit and, for example in the case of the bar, force stars onto specific orbital families. The underlying (static) Galactic potential can also cause 'observable' substructure in the space of orbital parameters. For example, Amarante et al. (2020) and Koppelman et al. (2021) have shown that the wedges seen in z_{\max} - r_{\max} space (see e.g. Haywood et al. 2018) are related to the transitions between different orbital families associated with resonances and chaotic regions in our galaxy.

How resonances and orbital families are populated in a system can in principle be used to constrain the form of its gravitational potential, for example the shape of its halo (Valluri et al. 2012). Furthermore, streams near a resonance may remain spatially coherent on longer timescales because their stars spread out more slowly (Vogelsberger et al. 2008). However, if the tidal debris is initially at the boundary between two orbital families (a separatrix), then, depending on the size of the system, the stars may evolve on widely different orbits and diverge much faster (Price-Whelan et al. 2016; Mestre et al. 2020; Yavetz et al. 2021), making such streams more difficult to detect. Understanding these different effects and mapping out the orbital resonances

in the Galactic potential is thus important for the identification and interpretation of substructures.

In this paper we revisit the Helmi streams' debris with the recently released *Gaia* Early Third Data Release (EDR3) data. First identified by Helmi et al. (1999, see also Chiba & Beers 2000; Kepley et al. 2007; Smith et al. 2009) and characterised further with *Gaia* Data Release 2 (DR2) by Koppelman et al. (2019a, hereafter K19), the Helmi streams are thought to be the debris of a massive dwarf galaxy, $M_* \sim 10^8 M_\odot$, that was accreted $\sim 5\text{--}8$ Gyr ago. Here we show that the stars' distribution in angular momentum space exhibits substructure, and we investigate its origin. We demonstrate that the stellar debris populations in the substructures are indistinguishable from one another and put forward the case that the substructure results from the presence of orbital resonances associated with the Galactic potential, particularly $\Omega_z/\Omega_\phi \sim 1$. We find, in fact, that if the flattening of the dark matter halo component in the McMillan (2017) Milky Way mass model is $q = 1.2$ (in the density), this ratio is exactly 1. We thus argue that this is likely the preferred shape of the halo for the region probed by the Helmi streams, namely within $\sim 5\text{--}20$ kpc of the Galactic centre.

This paper is structured as follows. Section 2 outlines the data used to select the Helmi streams, combining *Gaia* EDR3 with spectroscopic surveys. In Sect. 3 we present our results. Specifically, in Sect. 3.1 we show that all of the substructures in angular momentum space have consistent stellar populations, demonstrating that all of the stars are Helmi streams' debris. We explore the origin of the substructure in Sect. 3.2 using orbital frequency analysis (which is described in detail in Appendix A), while in Sect. 3.3 we demonstrate the sensitivity of the substructure to the flattening of the Galactic dark matter halo. Then in Sect. 4 we present our conclusions.

2. The data

2.1. Generalities

The latest data release of *Gaia*, EDR3, has provided more accurate proper motions and parallaxes and hence more accurate 6D phase-space information for nearby stars (Gaia Collaboration 2021). This dataset contains ~ 1.7 billion sources, of which 7 209 831 stars have the full 6D information (position on the sky, proper motions, parallax, and radial velocity from DR2). Selecting objects with `parallax_over_error > 5` and `RUWE < 1.4` leaves 5 709 139 stars within a 5 kpc volume around the Sun (and 4 496 187 within 2.5 kpc). We extended this sample with radial velocities from spatial cross-matches with the following spectroscopic surveys: APOGEE DR16 (Ahumada et al. 2020), LAMOST DR6 (Cui et al. 2012), Galah DR3 (Buder et al. 2021), and RAVE DR6 (Steinmetz et al. 2020). In total, this results in 9 148 793 stars in the 5 kpc volume (respectively, 7 531 934 within 2.5 kpc) with 6D phase-space information and high quality parallaxes. We used where possible the *Gaia*-measured radial velocities, supplemented then by Galah, APOGEE, RAVE, and finally LAMOST¹ in that order of preference. These spectroscopic surveys also provide metallicities [Fe/H] for some of the stars in this sample, and we used the LAMOST low resolution (LRS) metallicities for the analyses presented in this paper (because of the large numbers of targets and to ensure a uniform metallicity scale).

¹ The LAMOST LRS radial velocities have been corrected for the offset of 7.9 km s^{-1} with respect to the other surveys; see <http://dr6.lamost.org/v2/doc/release-note>

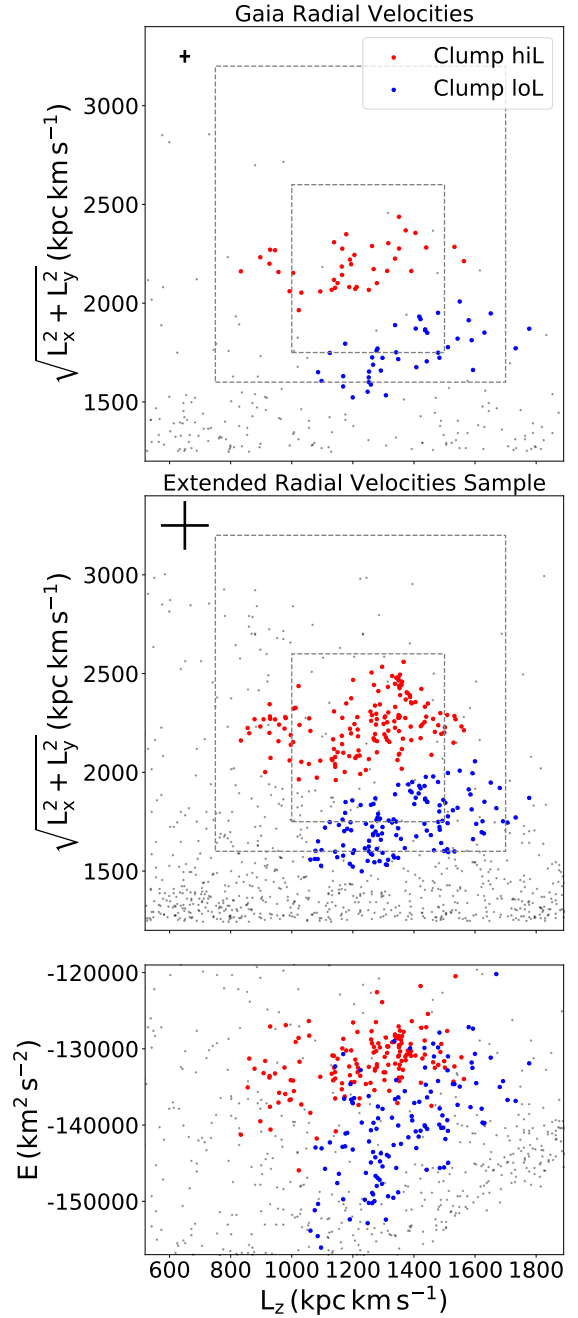


Fig. 1. Helmi streams' stars within 2.5 kpc are distributed in $L_z\text{--}L_\perp$ in two clumps: hiL (red) and loL (blue). The remainder of the stars in our halo sample in the 2.5 kpc volume are shown in black. Dashed lines show the selections used previously by K19 for the Helmi streams' debris. *Top panel:* stars with radial velocities from *Gaia*, *middle panel:* stars in the sample. The average uncertainties of the *Gaia* radial velocity sample (RVS) stars (27.7% of the extended sample) and the LAMOST LRS stars (60% of the extended sample) are shown by the black error bars in the *top* and *middle panel*, respectively. The uncertainties of the remaining stars in the sample (12.3%) are similar to those of the RVS. *Bottom panel:* shows how the stars are distributed in $L_z\text{--}E$ space.

The quality cut on the parallaxes allows us to use the inversion of the parallax to estimate the distance, after applying a zero point offset of $-17 \mu\text{as}$ (Lindegren et al. 2021). We corrected the stars for the solar motion using $(U, V, W)_\odot = (11.1, 12.24, 7.25) \text{ km s}^{-1}$ (Schönrich et al. 2010) and for the motion of the local standard of rest (LSR) using $v_{\text{LSR}} = 232.8 \text{ km s}^{-1}$

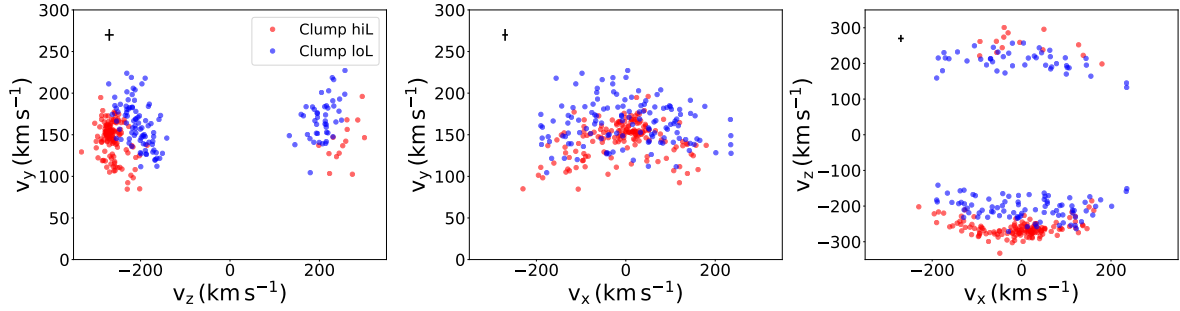


Fig. 2. Distribution in velocity space of the stars in clump-hiL (red) and clump-loL (blue) associated with the Helmi streams and located within 2.5 kpc. Both clumps populate the negative and positive v_z streams, which is characteristic of the Helmi streams’ debris. The average velocity uncertainties of these stars are shown by the black error bars in the top-left corner of each panel.

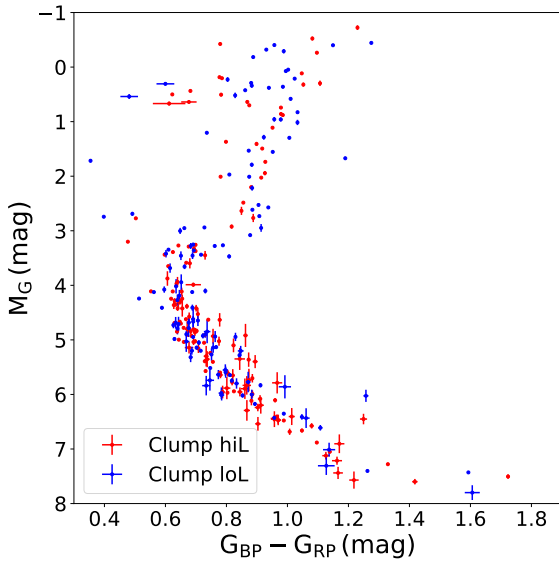


Fig. 3. Colour-absolute magnitude diagram of Helmi streams’ members within 2.5 kpc. Clump-hiL stars are shown in red and clump-loL in blue.

(McMillan 2017). Both the galactocentric Cartesian and cylindrical positions and velocities of the stars were calculated assuming $R_\odot = 8.2$ kpc (McMillan 2017) and $z_\odot = 0.014$ kpc (Binney et al. 1997). We defined the coordinate system such that x points towards the Galactic centre, y in the direction of motion of the disc, and positive (negative) z is the height above (below) the disc. Angular momenta, L_z and $L_\perp = \sqrt{L_x^2 + L_y^2}$, were calculated for the stars with the sign of L_z flipped such that it is positive for prograde orbits. Energy, E , is computed with AGAMA (Vasiliev 2019) and using the McMillan (2017) potential for the Milky Way. This potential is axisymmetric and made up of a stellar thin and thick disc, an HI gas disc, a molecular gas disc, a bulge, and a Navarro-Frenk-White (NFW) halo, which by default has a spherical shape.

2.2. Selection of the Helmi streams

Following K19, we selected the Helmi streams’ debris in L_z versus L_\perp space and applied a cut in energy of $E < -1.2 \times 10^5 \text{ km}^2 \text{ s}^{-2}$. Figure 1 shows the stars selected in this space compared to the entire sample, with the selections made in K19 outlined. When inspecting this by eye (or using a clustering algorithm; Lövdal et al., in prep.), it is clear that the debris separates out into two clumps, one with high L_\perp , which we name

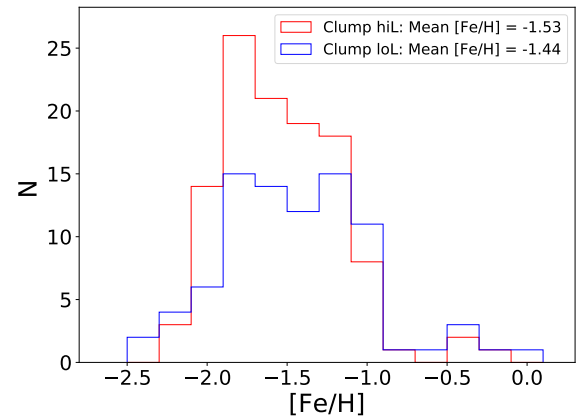


Fig. 4. Metallicity distributions for the stars in the Helmi streams in clump-hiL (red) and clump-loL (blue), where available from LAMOST LRS. Both clumps exhibit similar distributions, showing a broad range in metallicities that peak around $[\text{Fe}/\text{H}] \sim -1.5$.

clump-hiL (red), and one with a lower L_\perp , which we name clump-loL (blue). This figure includes all stars within a 2.5 kpc volume around the Sun, but the substructure is also present for stars with distances up to 5 kpc. The two clumps and the gap between them are most clearly seen in the top panel of Fig. 1, which includes stars with radial velocities from *Gaia* only and whose average radial velocity uncertainty is 2.1 km s^{-1} . The few stars in the middle panel of Fig. 1 that seem to populate the gap region, $L_\perp \sim 1800\text{--}2000 \text{ km s}^{-1}$, all have LAMOST LRS radial velocities and much larger average uncertainties of 12.7 km s^{-1} . The bottom panel of Fig. 1 shows that the two clumps overlap to some extent in L_z - E space.

We next proceeded to associate stars with each of the clumps as follows. Clump-hiL stars were selected using an ellipse centred on $(L_z, L_\perp) = (1225, 2255) \text{ kpc km s}^{-1}$ with major and minor axis lengths of 855 and 570 kpc km s^{-1} , respectively, rotated by an angle of 30 degrees anti-clockwise. Clump-loL stars were selected using an ellipse centred on $(L_z, L_\perp) = (1420, 1780) \text{ kpc km s}^{-1}$ with major and minor axis lengths of 860 and 430 kpc km s^{-1} , respectively, also rotated by an angle of 30 degrees anti-clockwise. There are 154 stars in clump-hiL and 130 stars in clump-loL within the 2.5 kpc volume. Although the remainder of the analysis presented is for this volume, we verified that the results remain valid for a larger volume of 5 kpc.

Figure 2 shows the Cartesian velocities of the stars colour-coded according to their membership to the clumps. Their velocity distributions are consistent with those previously reported for the Helmi streams. We observe negative and positive

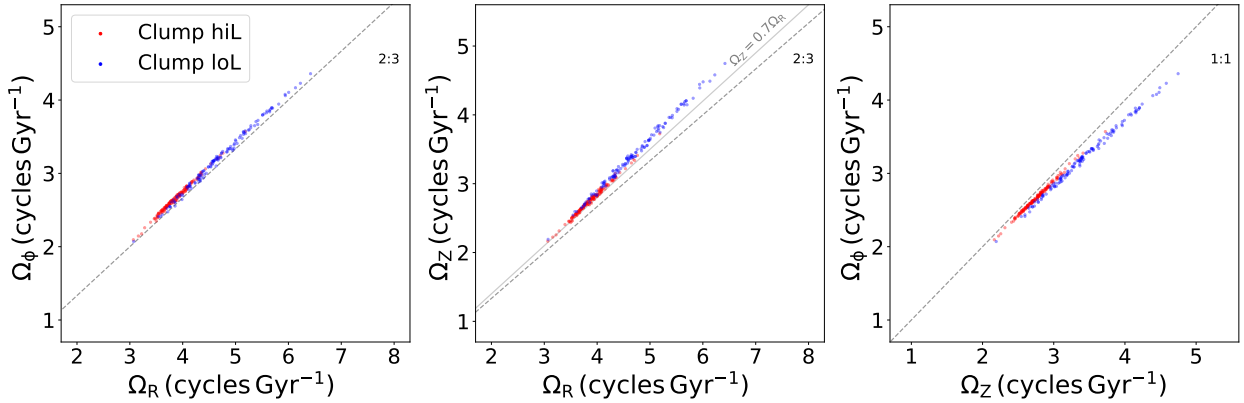


Fig. 5. Frequency space for the two angular momentum clumps. The red is clump-hiL (higher L_{\perp}) and the blue clump-loL. The dashed lines show the relevant resonances that the Helmi streams populate or come close to.

v_z kinematic groups that are populated in similar numbers by stars from the hiL and loL clumps. In fact, the asymmetry in the number of stars in the negative and positive v_z groups (previously used by K19 to estimate the time of accretion) remains, including when considering the two clumps in angular momentum. It should be noted that stars with lower L_{\perp} typically have lower $|v_z|$, since $L_{\perp} \sim R|v_z|$ at the location of the Sun. We also note that some of the stars in the hiL clump with negative v_z appear to be in a kinematically cold sub-clump. This tight group of clump-hiL stars likely corresponds to the S2 stream reported by Myeong et al. (2018) and can be seen to be simply part of the Helmi streams.

3. Results

3.1. Common origin

We now investigate the stellar populations and metallicity distributions of the two clumps in angular momentum space to establish if they have a common origin. Figure 3 shows the colour-absolute magnitude diagram (CaMD) of the two clumps, hiL and loL. We propagated the errors on the fluxes and parallax into errors on the colour ($G_{BP}-G_{RP}$) and M_G . The stars that have a six-parameter astrometric solution have had a correction applied to the G band photometry following Gaia Collaboration (2021). The observed magnitudes have also been corrected for extinction using the 2D Schlegel et al. (1998) dust map and applying the Gaia passband extinction coefficients² (Cardelli et al. 1989; O’Donnell 1994). Figure 3 reveals no differences in the CaMD of the clumps.

Both clumps also show similar metallicity distributions, as illustrated in Fig. 4, with clump-hiL (113 stars) having a mean $[Fe/H] \sim -1.53$ and clump-loL (86 stars) having ~ -1.44 , based on their LAMOST LRS $[Fe/H]$ measurements. A Kolmogorov–Smirnov test comparing the metallicity distributions of the two clumps yields a probability of 0.13 that the distributions are consistent with each other.

3.2. Frequency analysis

The analysis of the previous section demonstrates that the stars in the two angular momentum clumps have statistically indistinguishable stellar populations, and this supports a common origin. Thus, to explore the possible causes of the split in angular momentum space, we now investigate in more depth the

orbital properties of the two clumps. To this end, we integrated each star’s orbit in the McMillan (2017) potential with AGAMA (Vasiliev 2019). We integrated for ~ 100 Gyr in total, outputting the positions and velocities at regular time steps of ~ 1 Myr.

We investigated the frequencies of the orbits by using a variation on the cylindrical polar coordinates (namely Poincaré’s symplectic polar variables) following Valluri et al. (2012) and Koppelman et al. (2021). We inputted the positions and velocities in this coordinate system as complex time series into SuperFreq (Price-Whelan 2015), which numerically calculates the frequencies Ω_z , Ω_R , and Ω_{ϕ} . We defined Ω_{ϕ} to be positive for stars that orbit in the direction of Galactic rotation. We verified that the frequencies remain stable when splitting the full time interval into three equal sub-intervals, which indicates that the orbits are regular.

SuperFreq is an implementation of the Numerical Analysis of Fundamental Frequencies algorithm (originally pioneered by Laskar 1990, 1993) that determines the frequencies for the three components z , R , and ϕ . This is done by selecting the frequency with the highest amplitude in the Fourier transform of the time series. The resulting distributions of Ω_z and Ω_{ϕ} for the Helmi streams’ stars are well behaved, being relatively smooth and continuous, as expected. However, the distribution in Ω_R depicts two branches (see Fig. A.1), one of which (populated by 38% of the stars) seems to correspond to a $\Omega_z:\Omega_R = 1:2$ resonance. If we use an alternative implementation of this algorithm by Valluri & Merritt (1998) (see also Valluri et al. 2010, 2012), simply called NAFF, then only 10% of the stars are found to be located on the branch associated with this resonance. Inspection of the $R(t)$ for stars on and off the resonance do not warrant a significantly different Ω_R , nor do we see evidence that there is a resonance between R and z . Furthermore, we proceeded to action-angle space and determined the angular frequencies using the Stäckel fudge approximation implemented in AGAMA. In this case, we find a single branch and a continuous distribution of Ω_R for all the stars in the Helmi streams (see Appendix A for a detailed discussion). The frequency analysis performed by SuperFreq does identify what we would consider to be the true Ω_R but with slightly lower power. Thus, for these stars we chose to adopt the frequency in R that is of the second highest amplitude, such that all of the stars are on the same Ω_R branch and not on the $\Omega_z:\Omega_R = 1:2$ resonance.

Figure 5 shows the frequencies colour-coded by angular momentum clump. All of the stars in clump-hiL appear to be on a resonance close to $\Omega_{\phi}:\Omega_z \sim 1:1$, as can be seen in the third panel of Fig. 5. The histogram of Ω_{ϕ}/Ω_z for the entire 2.5 kpc

² http://stev.oapd.inaf.it/cgi-bin/cmd_3.4

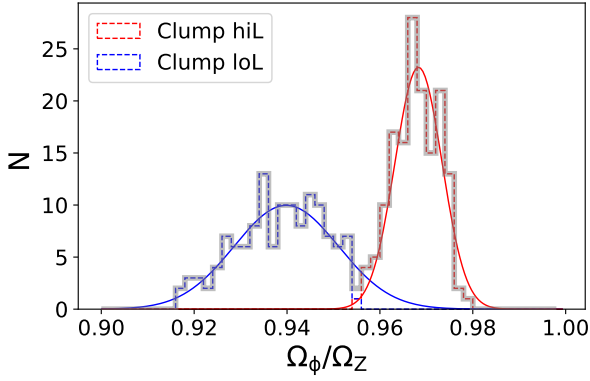


Fig. 6. Distribution of Ω_ϕ/Ω_z for all stars in the Helmi streams, with clump-hiL and clump-loL indicated in red and blue, respectively. The sum of two Gaussians fits their distributions well. Clump-hiL stars correspond to the tight component centred on $\Omega_\phi/\Omega_z = 0.968$ and clump-loL to the more diffuse component.

sample plotted in Fig. 6 clearly shows a peak corresponding to $\Omega_\phi:\Omega_z = 0.968:1$ with a thickness of ~ 0.015 . We fitted a sum of two Gaussian distributions to the histogram of Ω_ϕ/Ω_z and confirm that all of the stars in clump-hiL are located within three standard deviations of the mean of the component that represents this resonance. The second Gaussian component contains the clump-loL stars, which form a more diffuse cloud of stars at a slightly lower Ω_ϕ/Ω_z . We thus argue that the $\Omega_\phi:\Omega_z \sim 1:1$ resonance, which is associated with the gravitational potential, must be the cause of the substructure in angular momentum space.

3.3. A new constraint on the shape of the Galactic dark matter halo

In the chosen McMillan (2017) potential, the gap between the two clumps in angular momentum space remains visible over time, especially when considering only *Gaia* radial velocity stars, where the gap is clearest. Although L_\perp is not constant in this potential, its variation with time is not large enough to erase the gap (for over 2 Gyr) nor to move stars from one clump to the next (for at least 10 Gyr).

We verified that the Ω_ϕ/Ω_z resonance holds and is similarly populated when calculated with orbits integrated in various other potentials. In the Galactic potentials of Bovy (2015), Piffl et al. (2014), and Price-Whelan (2017), the clump-hiL stars correspond to the tighter group of stars that are on a $\Omega_\phi:\Omega_z$ resonance close to 1:1. In the static triaxial Vasiliev et al. (2021) potential³, a branch close to the above-mentioned resonance is apparent, although it is more diffuse. More importantly, the gap in angular momentum space disappears after <100 Myr of the orbit integration. This suggests that this model provides a less accurate representation of the Galactic potential in the region probed by the orbits of the Helmi stream stars if we make the reasonable assumption that we are not living at a special time in Galactic history.

In order to investigate if there is any sensitivity to the shape of the Galactic halo as suggested by Valluri et al. (2012), we introduced flattening into the dark matter halo component of the McMillan (2017) potential. The density of this component follows the NFW form:

³ We used the fiducial model with a static twisted halo and no Large Magellanic Cloud, which these authors suggest is the best static potential fitted on the Sagittarius stream.

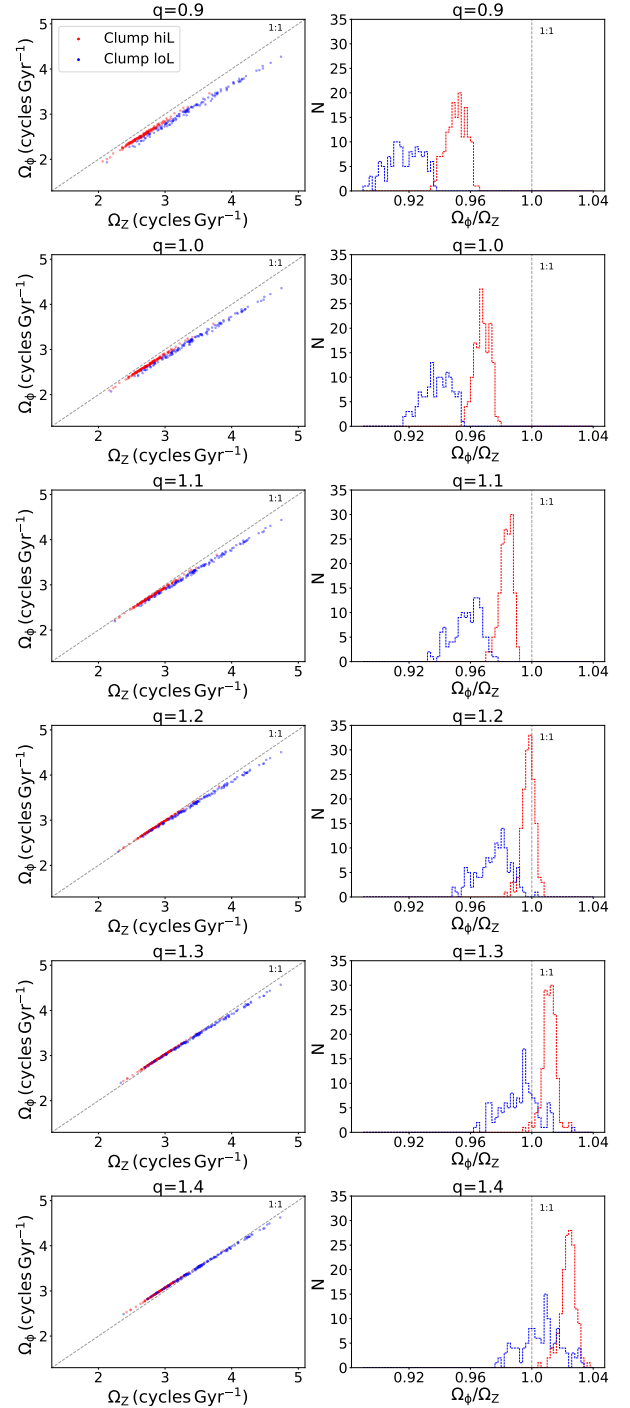


Fig. 7. Frequency, Ω_ϕ and Ω_z , distributions (left column) and histograms of their ratios (right column) for all stars in the Helmi streams. Clump-hiL and Clump-loL stars are shown in red and blue, respectively. Each row shows a different flattening added to the McMillan (2017) halo component, with the axis ratio, q , increasing from 0.9 (oblate) to 1.4 (prolate).

$$\rho = \rho_o \left(\frac{\tilde{r}}{a} \right)^{-1} \left[1 + \frac{\tilde{r}}{a} \right]^{-2},$$

where

$$\tilde{r} = \sqrt{x^2 + y^2 + \left(\frac{z}{q} \right)^2},$$

$$\rho_o = 8.53702 \times 10^6 M_\odot \text{ kpc}^{-3}, \text{ and } a = 19.5725 \text{ kpc}.$$

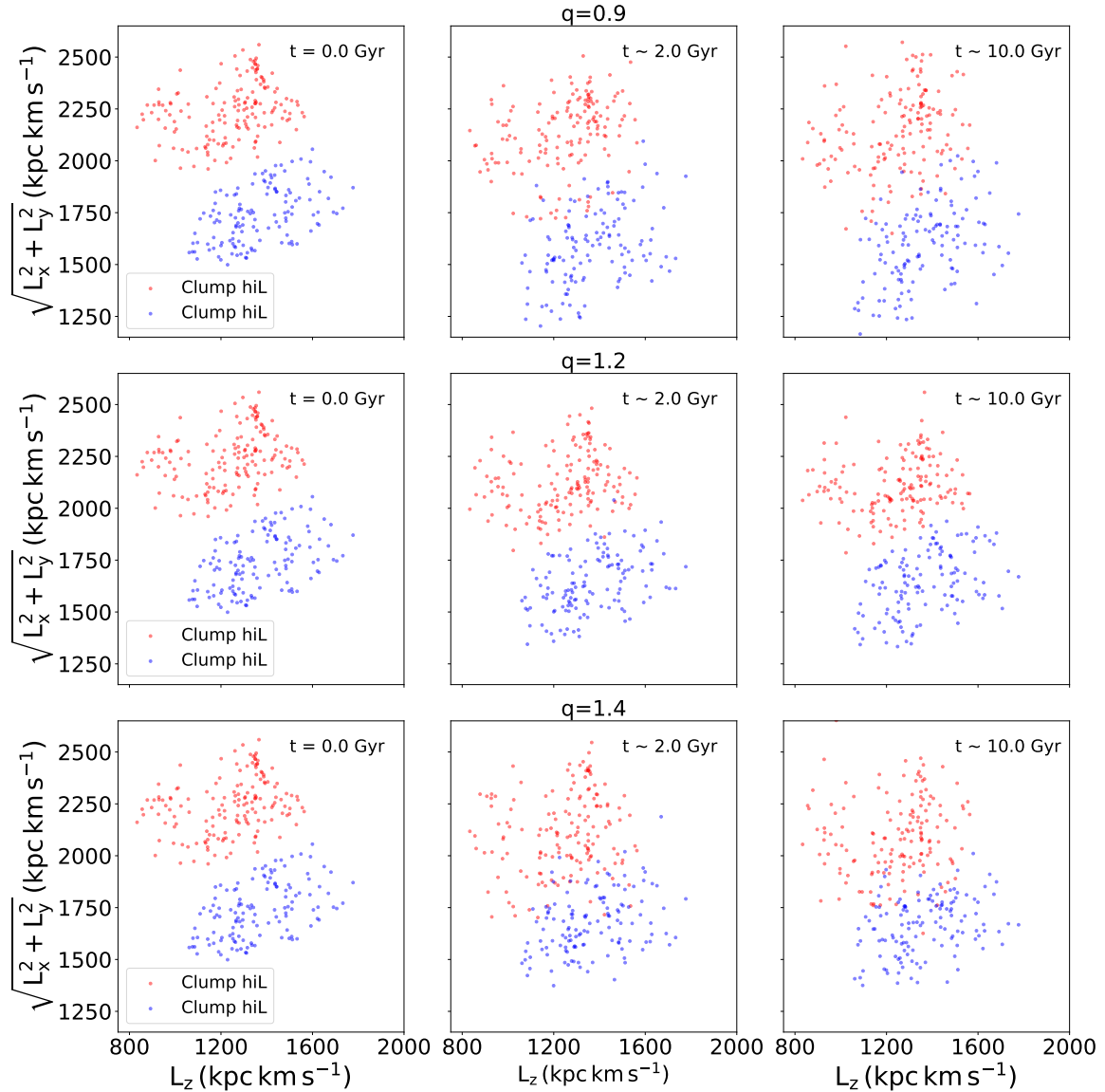


Fig. 8. Evolution of $L_z - L_\perp$ over time in the [McMillan \(2017\)](#) potential with various values of the flattening, q (in the density), of the halo component. The *first column* shows the present-day observed distribution in $L_z - L_\perp$, the *second column* the stars in $L_z - L_\perp$ space after ~ 2 Gyr integration time, and the *third column* after ~ 10 Gyr. The *first row* shows the results for the model with the lowest q (0.9) and the *bottom row* the highest q , with the best estimate, $q = 1.2$, shown in the *middle row*.

We varied q (the density axis ratio of z to R) from 0.9 to 1.4 in steps of 0.1. We then integrated the orbits of all stars in these different potentials and calculated the orbital frequencies as before (see Sect. 3.2). The different rows in Fig. 7 show the results. As q increases, the resonance that the clump-hiL stars occupy moves closer to the $\Omega_z : \Omega_\phi = 1:1$, up until $q = 1.2$, after which the stars move past the 1:1. The distribution of the clump-hiL stars in $\Omega_z - \Omega_\phi$ space also gets narrower and more peaked as q increases up to $q = 1.2$, as can be seen in the second column of Fig. 7.

We also find that as we reduce the flattening of the halo component ($q = 0.9$), the gap in L_z and L_\perp is no longer conserved and stars move from one clump to another (see the first row of Figs. 8 and 9). As q increases above 1.0 and the dark matter halo becomes more elongated, there is less mixing of stars and the gap is maintained better. This is true up until $q = 1.2$, for which we see the least amount of mixing and that the gap is best conserved. This can be seen in the middle row of Figs. 8 and 9. As we increase q further ($q > 1.2$), the mixing of stars increases and

the gap disappears, as shown in the bottom row of Figs. 8 and 9 for $q = 1.4$.

Since L_z and L_\perp can be computed directly from the observables without knowledge of the Galactic potential, but their evolution in time depends on the specific functional form, the presence of two clumps, or a long-lasting gap, serves to directly constrain the shape of the potential. Our analysis suggests that the dark matter halo component of the Galaxy in the region probed by the Helmi streams (within ~ 20 kpc) has an elongated shape with a density z/R axis ratio of ~ 1.2 . The shape of the dark matter halo is thought to be oblate or spherical in the central regions (e.g. [Koposov et al. 2010](#)) and to gradually become more triaxial with its major axis along z at larger radii (e.g. [Law & Majewski 2010](#)), possibly with a varying flattening as a function of radius (e.g. [Vera-Ciro & Helmi 2013](#)). Our new constraint at an intermediate radius is in close agreement with measurements using Galactic globular clusters as tracers, which probe similar radii as the Helmi streams' orbits ($q = 1.30 \pm 0.25$, [Posti & Helmi 2019](#)).

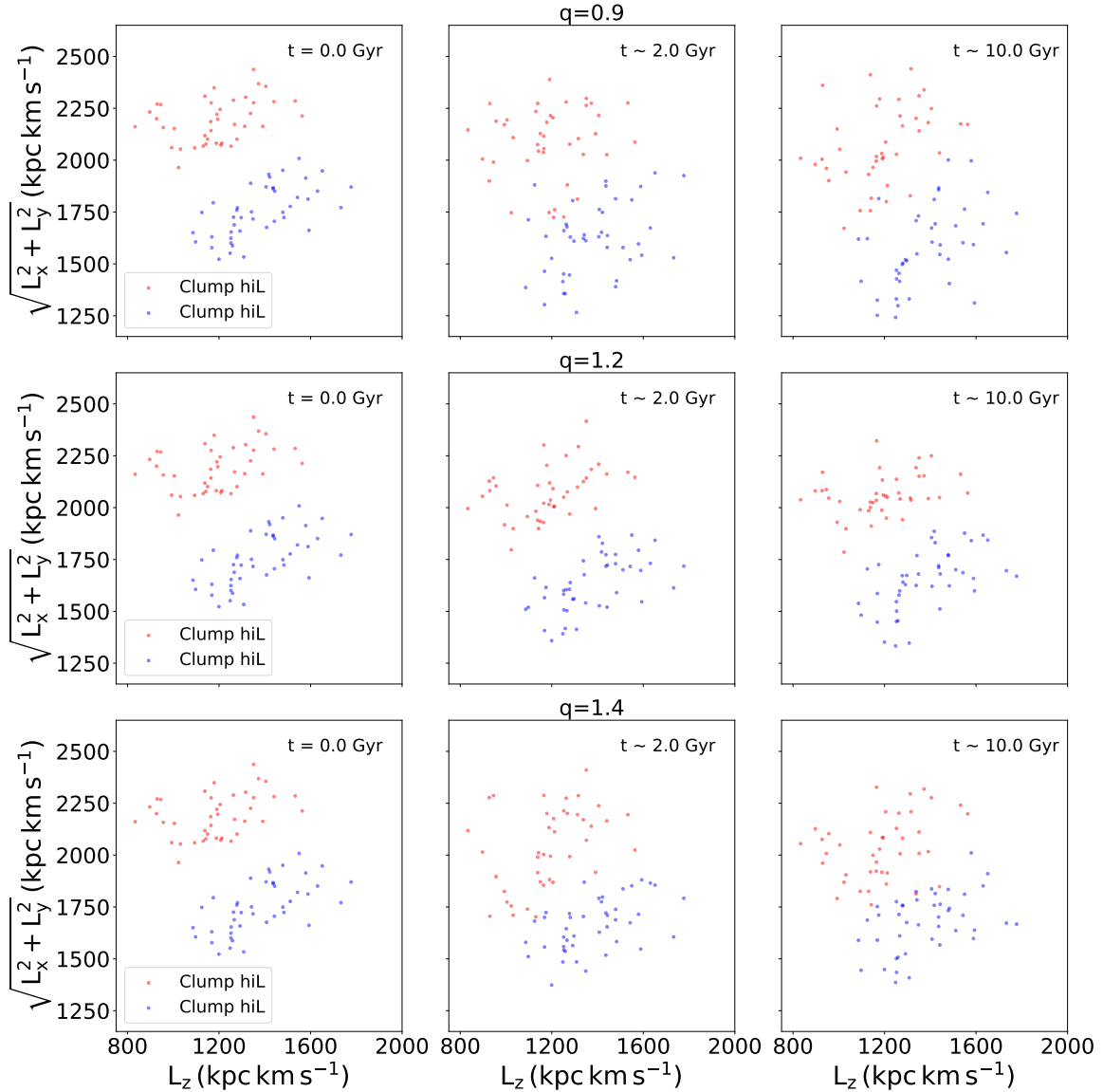


Fig. 9. Same as Fig. 8, but for the *Gaia* radial velocity sample that has significantly lower uncertainties.

4. Discussion and conclusions

We have shown that the local Helmi streams’ debris is divided into two clumps in L_z-L_\perp space, most clearly for stars within 2.5 kpc of the Sun. The stars in these clumps most likely share the same progenitor as their stellar populations are indistinguishable. We have determined that the origin of this substructure in angular momentum space is related to the presence of an orbital resonance. Specifically, the stars in the high- L_\perp clump are on a $\Omega_\phi:\Omega_z$ resonance located very close to the 1:1 resonance, while the remaining stars show a broader range of frequencies. In $\Omega_R-\Omega_z$ all of the stars are distributed close to $\Omega_z/\Omega_R \sim 0.7$.

We have used the Helmi streams’ debris to put a constraint on the shape of the dark matter halo. Our findings suggest that the dark matter halo within $\sim 5-20$ kpc of the Galactic centre is elongated along the axis perpendicular to the disc (z) with a value of $q \sim 1.2$ (in the density). Evidence for this value of q arises from the fact that the stars in the high- L_\perp clump form the tightest distribution, populating the $\Omega_\phi:\Omega_z = 1:1$ resonance, but are broader and offset from this integer ratio for other values of q . Furthermore, the evolution of the clumps and the gap in L_z-L_\perp

space is longest-lived and depicts the least amount of mixing for $q = 1.2$.

We have presented the analysis of the streams for the stars located within 2.5 kpc, but we find similar results when we go farther away, up to 5 kpc from the Sun. Going to larger volumes with the Helmi streams is a possible way to map out the local potential. We have demonstrated how L_z-L_\perp space can be useful in constraining the potential. This is probably the first time that a ‘direct’ observable has been used in this way, specifically for halo stars and linking with a particular resonance in frequency space.

The presence of such rich structure in terms of different resonant families in a small region of phase space (i.e. that occupied by the Helmi streams) may force us to rethink how we model the evolution of streams. If stars in a stream are on a resonance, they remain coherent for longer, but if they are just off a resonance and the stream stars’ orbits fall on either side of a resonant orbit, then the stars are affected and the stream diverges very quickly (e.g. Yavetz et al. 2021). When we model streams, we do not take the effect of resonant orbits into account and simply assume that they are on regular orbits.

Our findings also add to the evidence that there can be substructure in the orbital properties and notably in integrals of motion space that is not a result of accretion but an effect of the Galactic potential. If single progenitors are splitting up in this manner, then this further complicates the identification (and characterisation) of their phase-mixed debris. Furthermore, frequency space has been argued to be useful in constraining the time of accretion since merger debris separates into a regular pattern in this space, associated with each individual stream crossing the specific volume being considered (e.g. Gómez & Helmi 2010). Although we do see evidence of multiple small clumps potentially associated with such individual streams, the presence of resonances inducing further substructures complicates the prospects of straightforwardly using this idea.

Several questions remain on the origin of these different resonances, for example whether there is a link to Sagittarius. Previously, Koppelman et al. (2021) showed using also the McMillan potential that Sagittarius' orbit falls on the $\Omega_\phi:\Omega_z = 1:1$ resonance, suggesting that there may be some relation between the dynamics of Sgr and the orbits of the Helmi streams' debris. On the other hand, streams on prograde orbits could also be affected by the Galactic bar, as demonstrated by Pearson et al. (2017).

Acknowledgements. We would like to thank the anonymous referee for their contributions to this article. We also thank Leandro Beraldo e Silva (and Monica Valluri) for the helpful discussions and guidance in using NAFF. We acknowledge financial support from a Spinoza prize to AH. H.H.K. gratefully acknowledges support from the Martin A. and Helen Chooljian Membership at the Institute for Advanced Study. This work has made use of data from the European Space Agency (ESA) mission *Gaia* (<https://www.cosmos.esa.int/gaia>), processed by the *Gaia* Data Processing and Analysis Consortium (DPAC, <https://www.cosmos.esa.int/web/gaia/dpac/consortium>). Funding for the DPAC has been provided by national institutions, in particular the institutions participating in the *Gaia* Multilateral Agreement. The analysis has benefited from the use of the following packages: vaex (Breddels & Veljanoski 2018), SuperFreq (Price-Whelan 2017), NAFF (Valluri & Merritt 1998; Valluri et al. 2010, 2012), AGAMA (Vasiliev 2019), numpy (Van Der Walt et al. 2011), matplotlib (Hunter 2007) and jupyter notebooks (Kluyver et al. 2016).

References

- Ahumada, R., Prieto, C. A., Almeida, A., et al. 2020, *ApJS*, 249, 3
- Amarante, J. A., Smith, M. C., & Boeche, C. 2020, *MNRAS*, 492, 3816
- Antoja, T., Helmi, A., Romero-Gómez, M., et al. 2018, *Nature*, 561, 360
- Belokurov, V., Erkal, D., Evans, N., Koposov, S., & Deason, A. 2018, *MNRAS*, 478, 611
- Binney, J. 2012, *MNRAS*, 426, 1324
- Binney, J., Gerhard, O., & Spergel, D. 1997, *MNRAS*, 288, 365
- Bovy, J. 2015, *ApJS*, 216, 29
- Breddels, M. A., & Veljanoski, J. 2018, *A&A*, 618, A13
- Brook, C. B., Kawata, D., Gibson, B. K., & Flynn, C. 2002, *ApJ*, 585, L125
- Buder, S., Sharma, S., Kos, J., et al. 2021, *MNRAS*, 506, 150
- Cardelli, J. A., Clayton, G. C., & Mathis, J. S. 1989, *ApJ*, 345, 245
- Chiba, M., & Beers, T. C. 2000, *AJ*, 119, 2843
- Cui, X.-Q., Zhao, Y.-H., Chu, Y.-Q., et al. 2012, *Res. Astron. Astrophys.*, 12, 1197
- Dehnen, W. 2000, *AJ*, 119, 800
- Gaia Collaboration (Brown, A. G. A., et al.) 2018, *A&A*, 616, A1
- Gaia Collaboration (Brown, A. G. A., et al.) 2021, *A&A*, 649, A1
- Gómez, F. A., & Helmi, A. 2010, *MNRAS*, 401, 2285
- Hayes, C. R., Majewski, S. R., Shetrone, M., et al. 2018, *ApJ*, 852, 49
- Haywood, M., Di Matteo, P., Lehner, M., et al. 2018, *ApJ*, 863, 113
- Helmi, A. 2020, *ARA&A*, 58, 205
- Helmi, A., & de Zeeuw, P. T. 2000, *MNRAS*, 319, 657
- Helmi, A., White, S. D., De Zeeuw, P. T., & Zhao, H. 1999, *Nature*, 402, 53
- Helmi, A., Babusiaux, C., Koppelman, H. H., et al. 2018, *Nature*, 563, 85
- Hunter, J. D. 2007, *IEEE Ann. Hist. Comput.*, 9, 90
- Kepley, A. A., Morrison, H. L., Helmi, A., et al. 2007, *AJ*, 134, 1579
- Kluyver, T., Ragan-Kelley, B., Pérez, F., et al. 2016, *Jupyter Notebooks—A Publishing Format for Reproducible Computational Workflows* (IOS Press), 87
- Koposov, S. E., Rix, H.-W., & Hogg, D. W. 2010, *ApJ*, 712, 260
- Koppelman, H., Helmi, A., & Veljanoski, J. 2018, *ApJ*, 860, L11
- Koppelman, H. H., Helmi, A., Massari, D., Roelenga, S., & Bastian, U. 2019a, *A&A*, 625, A5
- Koppelman, H. H., Helmi, A., Massari, D., Price-Whelan, A. M., & Starkenburg, T. K. 2019b, *A&A*, 631, L9
- Koppelman, H. H., Hagen, J. H., & Helmi, A. 2021, *A&A*, 647, A37
- Laporte, C. F., Johnston, K. V., Gómez, F. A., Garavito-Camargo, N., & Besla, G. 2018, *MNRAS*, 481, 286
- Laporte, C. F., Minchev, I., Johnston, K. V., & Gómez, F. A. 2019, *MNRAS*, 485, 3134
- Laskar, J. 1990, *Icarus*, 88, 266
- Laskar, J. 1993, *Celest. Mech. Dyn. Astron.*, 56, 191
- Law, D. R., & Majewski, S. R. 2010, *ApJ*, 718, 1128
- Lindgren, L., Bastian, U., Biermann, M., et al. 2021, *A&A*, 649, A4
- McMillan, P. J. 2017, *MNRAS*, 465, 76
- Mestre, M., Llinares, C., & Carpintero, D. D. 2020, *MNRAS*, 492, 4398
- Meza, A., Navarro, J. F., Abadi, M. G., & Steinmetz, M. 2005, *MNRAS*, 359, 93
- Myeong, G., Evans, N., Belokurov, V., Amorisco, N., & Koposov, S. 2018, *MNRAS*, 475, 1537
- Myeong, G., Vasiliev, E., Iorio, G., Evans, N., & Belokurov, V. 2019, *MNRAS*, 488, 1235
- Naidu, R. P., Conroy, C., Bonaca, A., et al. 2020, *ApJ*, 901, 48
- Naidu, R. P., Conroy, C., Bonaca, A., et al. 2021, *ApJ*, 923, 92
- Nissen, P. E., & Schuster, W. J. 2010, *A&A*, 511, L10
- O'Donnell, J. E. 1994, *ApJ*, 422, 158
- Pearson, S., Price-Whelan, A. M., & Johnston, K. V. 2017, *Nat. Astron.*, 1, 633
- Piffl, T., Binney, J., McMillan, P. J., et al. 2014, *MNRAS*, 445, 3133
- Posti, L., & Helmi, A. 2019, *A&A*, 621, A56
- Price-Whelan, A. M. 2015, *Astrophysics Source Code Library* [record ascl:1511.001]
- Price-Whelan, A. M. 2017, *J. Open Sour. Softw.*, 2, 388
- Price-Whelan, A. M., Johnston, K. V., Valluri, M., et al. 2016, *MNRAS*, 455, 1079
- Ramos, P., Antoja, T., & Figueras, F. 2018, *A&A*, 619, A72
- Schlegel, D. J., Finkbeiner, D. P., & Davis, M. 1998, *ApJ*, 500, 525
- Schönrich, R., Binney, J., & Dehnen, W. 2010, *MNRAS*, 403, 1829
- Smith, M., Evans, N., Belokurov, V., et al. 2009, *MNRAS*, 399, 1223
- Steinmetz, M., Matijević, G., Enke, H., et al. 2020, *AJ*, 160, 82
- Valluri, M., & Merritt, D. 1998, *ApJ*, 506, 686
- Valluri, M., Debattista, V. P., Quinn, T., & Moore, B. 2010, *MNRAS*, 403, 525
- Valluri, M., Debattista, V. P., Quinn, T. R., Roškar, R., & Wadsley, J. 2012, *MNRAS*, 419, 1951
- Van Der Walt, S., Colbert, S. C., & Varoquaux, G. 2011, *Comput. Sci. Eng.*, 13, 22
- Vasiliev, E. 2019, *MNRAS*, 482, 1525
- Vasiliev, E., Belokurov, V., & Erkal, D. 2021, *MNRAS*, 501, 2279
- Vera-Ciro, C., & Helmi, A. 2013, *ApJ*, 773, L4
- Vogelsberger, M., White, S. D., Helmi, A., & Springel, V. 2008, *MNRAS*, 385, 236
- Yavetz, T. D., Johnston, K. V., Pearson, S., Price-Whelan, A. M., & Weinberg, M. D. 2021, *MNRAS*, 501, 1791

Appendix A: Comparison of methods for frequency determination

Here we compare three different methods for determining the orbital frequencies. Presented earlier in the paper are the frequencies determined with SuperFreq (Price-Whelan 2015), which is one implementation of the Numerical Analysis of Fundamental Frequencies algorithm. We observed that using this method the stars form two branches in Ω_R . This can be seen in Fig. A.1, where the stars on the higher Ω_R branch are those on the $\Omega_Z:\Omega_R = 1:2$ resonance. Figure A.1 shows that stars with the same energy (and very similar angular momenta) have very different Ω_R .

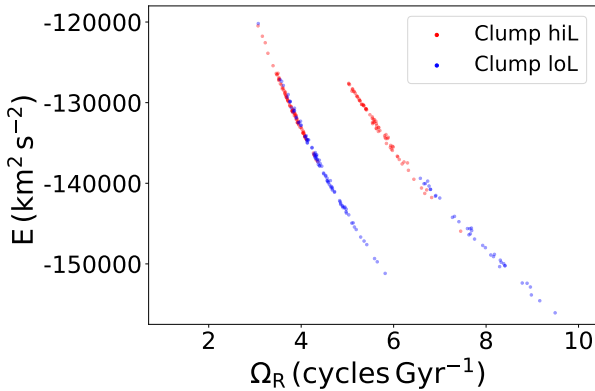


Fig. A.1. Distribution of radial frequencies, Ω_R , from SuperFreq, with energy coloured according to L_z-L_\perp clump. Two branches can be seen clearly. The branch at higher Ω_R corresponds to the stars that are placed onto the $\Omega_Z:\Omega_R = 1:2$ resonance.

Another implementation of the Numerical Analysis of Fundamental Frequencies algorithm is NAFF by Valluri & Merritt (1998) (see also Valluri et al. 2010, 2012). As already mentioned, we find differences in Ω_R for a significant fraction of the stars when comparing these two methods. Specifically, 28% of the stars move from the resonance in $\Omega_Z:\Omega_R$ to the branch closer to $\Omega_Z/\Omega_R \sim 0.7$. For all stars, both methods show peaks in the frequency spectrum of Ω_R that would place the star on the $\Omega_Z:\Omega_R = 1:2$ resonance or on the $\Omega_Z/\Omega_R \sim 0.7$ branch. In some cases, the amplitudes of these two peaks are very similar, which is possibly why there may be some discrepancy in the true Ω_R .

An alternative method is to determine the frequencies (Ω_i) analytically from the actions (J_i) using $\Omega_i = \delta H / \delta J_i$, where H is the Hamiltonian. This can be done for a Stäckel potential. We can approximate the McMillan (2017) potential to be a Stäckel potential at different points along an orbit and analytically solve for the frequencies at each point. This method is known as the Stäckel fudge method (Binney 2012). We used ActionFinder from AGAMA (Vasiliev 2019) with the orbit inputted as $R(t)$, $z(t)$, $\phi(t)$. ActionFinder implements the Stäckel fudge method and gives an approximation for the actions, angles, and frequencies that vary along the orbit. We then took the average over the full orbit for each star to be the frequency. The frequencies derived in this way show only one single branch in Ω_R but the same distributions in Ω_Z and Ω_ϕ . We verified that the variations in Ω_R along the orbit are not large enough to move the stars from one branch to the $\Omega_Z:\Omega_R = 1:2$ resonance. We thus argue that the Ω_R determined by SuperFreq and NAFF for the stars that are placed on the 1:2 resonance are not the true frequencies. For these stars, we took the Ω_R frequency with the second highest amplitude

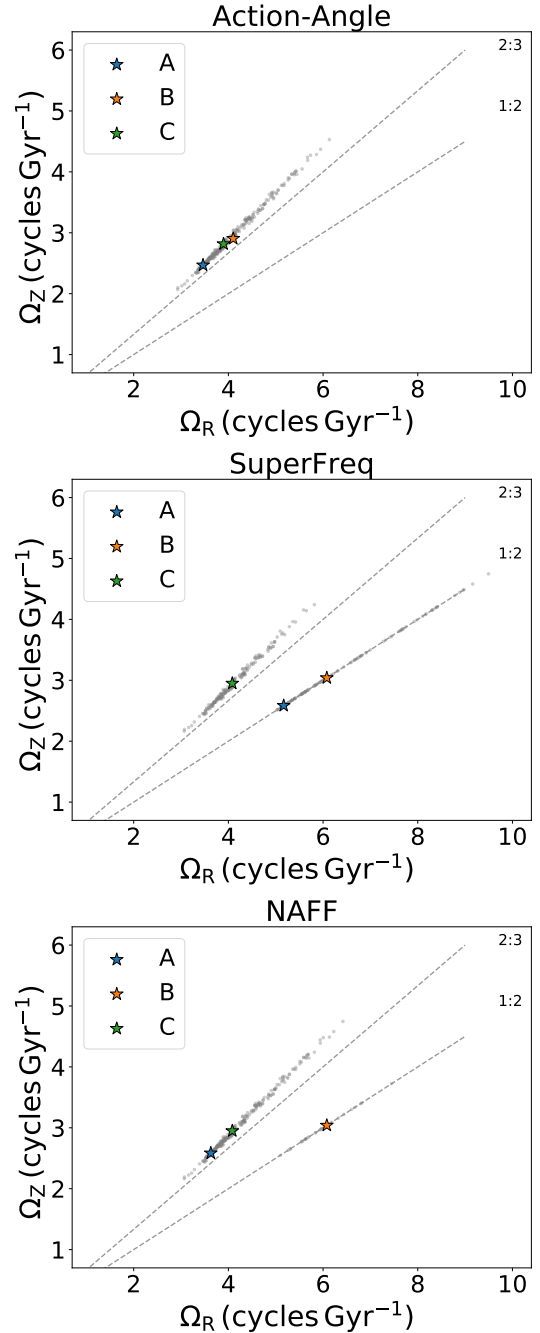


Fig. A.2. Comparison of Ω_R - Ω_Z frequencies determined by several different methods. The first row shows the frequencies determined using the action-angle method (in grey), with three selected stars (A, B, and C) indicated by coloured star symbols. These three stars are also depicted in the following two rows, which show the SuperFreq- and NAFF-determined frequencies, respectively. Star A (blue) is determined to be on the $\Omega_Z/\Omega_R = 0.7$ branch both for the action-angle frequencies and by NAFF. However, SuperFreq disagrees, placing this star on the 1:2 resonance. Star B (orange) is on the $\Omega_Z/\Omega_R = 0.7$ branch for the action-angle frequencies only, but NAFF and SuperFreq place this star on the 1:2 resonance. Finally, star C (green) is on the $\Omega_Z/\Omega_R = 0.7$ branch in all three methods.

in the frequency spectrum, which places the stars onto a single branch (the $\Omega_Z/\Omega_R \sim 0.7$ branch).

We can further demonstrate the differences in the Ω_R values determined by these methods using three example stars: A, B, and C. Figure A.2 shows these three stars in Ω_R - Ω_Z space. Star A

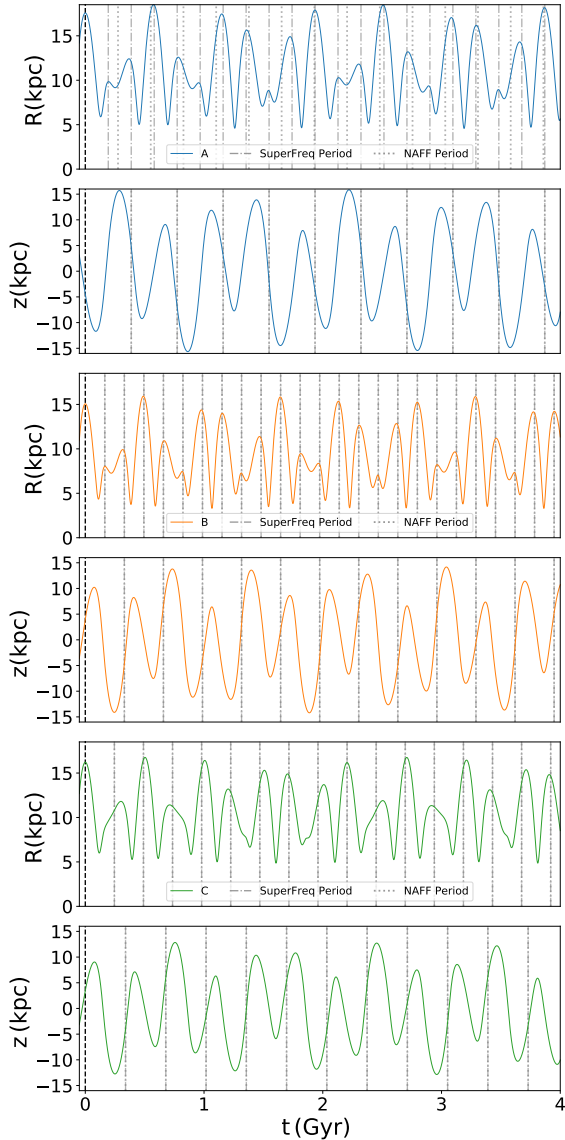


Fig. A.3. Evolution of R and z with time for the orbit integrations of the three selected stars: A, B, and C. Each star's $R(t)$ is shown over a period of 4 Gyr, with $t = 0$ Gyr set to the first maximum such that the three stars are in phase. The $z(t)$ is shown over the same time period for the corresponding star. Grey dash-dot and dotted lines correspond to the periods according to the frequencies derived by SuperFreq and NAFF, respectively.

corresponds to a star that is on the 1:2 resonance in SuperFreq but on the single branch with both NAFF and the action-angle frequencies. Star B is a star that is on the 1:2 resonance with both SuperFreq and NAFF, but on the single branch with the action-angles. Finally, star C is a star that is on the single branch in Ω_R for all three methods.

In Fig. A.3 we show the evolution of R and z with time for the orbit integrations of these three stars. We show the stars over a time period of 4 Gyr, with $t = 0$ Gyr set to the first peak such that the three stars are in phase to aid comparison. Periods are shown

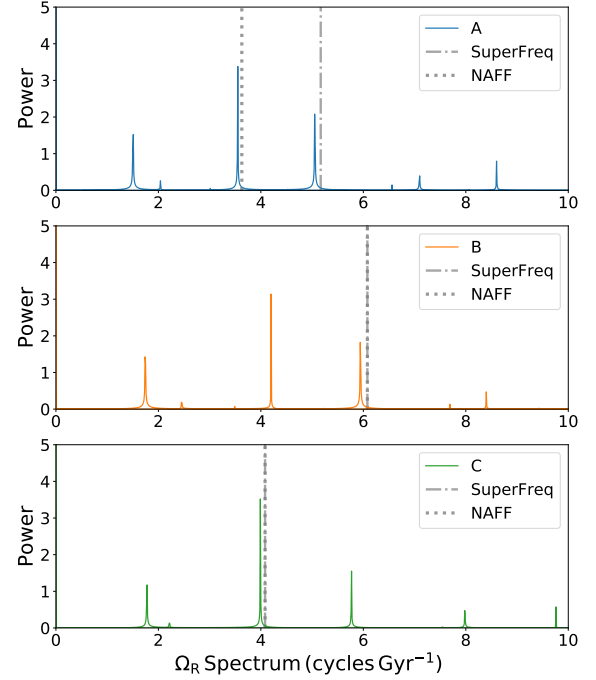


Fig. A.4. Fast Fourier transform of $R(t)$ for the full ~ 100 Gyr orbit integration of the three selected stars: A, B, and C. Grey dash-dot and dotted lines correspond to the frequencies derived by SuperFreq and NAFF, respectively. All three stars show a peak at $\Omega_R \sim 4$, which would place the star on the single Ω_Z - Ω_R branch, and another peak at a slightly higher frequency, which places the star on the 1:2 resonance.

with lines according to the frequencies derived by SuperFreq and NAFF. For both stars B and C the two methods agree, and so these lines overlap. However, for star A the periods do not line up, though we do see them overlap as the overall pattern in $R(t)$ repeats ($t \sim 2$ Gyr). Comparing the three stars $R(t)$ shown in Fig. A.3, it is not clear that the stars should have as different Ω_R values as suggested by the frequency identification methods.

Figure A.4 shows the fast Fourier transform (FFT) of $R(t)$ for the three stars along with the frequencies determined by SuperFreq and NAFF. There is not a clear difference between these three frequency spectra or an indication as to why a method prefers the higher frequency in some cases, placing it on the 1:2 resonance. The frequency spectrum shown in Fig. A.4 is derived from $R(t)$ only, whereas SuperFreq and NAFF take the complex time series of $R(t) + iV_R(t)$. We use Fig. A.4 simply to illustrate the two peaks and show that there are no differences in $R(t)$ that would indicate the difference in Ω_R . If we instead look at the SuperFreq frequency spectrum, then the main differences that we observe, compared to our FFT (Fig. A.4), are that the amplitudes of the Ω_R peaks change. For stars A and B, the FFT (Fig. A.4) shows the highest amplitude at the frequency that would place the star on the $\Omega_Z/\Omega_R = 0.7$ branch. However, the SuperFreq frequency spectrum shows the highest amplitude at higher Ω_R , the Ω_R that places them onto the 1:2 resonance.

We also note that stars B and C have very similar energy, and so it is unrealistic for the two stars to have as big a difference in Ω_R as SuperFreq and NAFF suggest.